

Fluorescent nanodiamonds as innovative delivery systems for MiR-34a replacement in breast cancer

Marianna Abate,^{1,7,8} Angela Lombardi,^{1,8} Amalia Luce,¹ Manuela Porru,² Carlo Leonetti,² Marco Bocchetti,^{1,3} Virginia Campani,⁴ Giuseppe De Rosa,⁴ Sossio Fabio Graziano,⁴ Valeria Nele,⁴ Francesco Cardile,³ Federica Zito Marino,⁵ Renato Franco,⁵ Andrea Ronchi,⁵ Marianna Scrima,³ Rossella Sperlongano,¹ Roberto Alfano,⁶ Gabriella Misso,¹ Evzen Amler,^{1,7} Michele Caraglia,^{1,3} and Silvia Zappavigna¹

¹Department of Precision Medicine, University of Campania “Luigi Vanvitelli,” Via L. De Crechchio 7, 80138 Naples, Italy; ²Translational Oncology Research Unit, IRCCS Regina Elena National Cancer Institute, E Chianesi 53, 00144 Rome, Italy; ³Laboratory of Precision and Molecular Oncology, Biogem Scarl, Institute of Genetic Research, Contrada Camporeale, 83031 Ariano Irpino, Italy; ⁴Department of Pharmacy, University of Naples Federico II, D. Montesano 49, 80131 Naples, Italy; ⁵Department of Mental and Physical Health and Preventive Medicine, Pathology Unit, University of Campania “Luigi Vanvitelli,” 80138 Naples, Italy; ⁶Department of Advanced Medical and Surgical Sciences “DAMSS,” University of Campania “Luigi Vanvitelli,” Via S. M. di Costantinopoli 104, 80138 Naples, Italy; ⁷Institute of Biophysics, 2nd Faculty of Medicine, Charles University, V Uvalu 84, 15006 Prague, Czech Republic

Nanodiamonds are innovative nanocrystalline carbon particles able to deliver chemically conjugated miRNAs. In oncology, the use of miRNA-based therapies may represent an advantage, based on their ability to simultaneously target multiple intracellular oncogenic targets. Here, nanodiamonds were tested and optimized to deliver miR-34a, a miRNA playing a key role in inhibiting tumor development and progression in many cancers. The physical-chemical properties of nanodiamonds were investigated suggesting electrical stability and uniformity of structure and size. Moreover, we evaluated nanodiamond cytotoxicity on two breast cancer cell models and confirmed their excellent biocompatibility. Subsequently, nanodiamonds were conjugated with miR-34a, using the chemical crosslinker polyethyleneimine; real-time PCR analysis revealed a higher level of miR-34a in cancer cells treated with the different formulations of nanodiamonds than with commercial transfectant. A significant and early nanodiamond-miR-34a uptake was recorded by FACS and fluorescence microscopy analysis in MCF7 and MDA-MB-231 cells. Moreover, nanodiamond-miR-34a significantly inhibited both cell proliferation and migration. Finally, a remarkable anti-tumor effect of miR-34a-conjugated nanodiamonds was observed in both heterotopic and orthotopic murine xenograft models. In conclusion, this study provides a rationale for the development of new therapeutic strategies based on use of miR-34a delivered by nanodiamonds to improve the clinical treatment of neoplasms.

INTRODUCTION

In last decades, nanotechnologies have played a central role in scientific research; in particular, the use of nanoparticles revealed revolutionary perspectives in medical-diagnostic¹ and therapeutic fields.^{2–4}

High surface/volume ratio and nanometric dimensions are typical chemical-physical characteristics of nanoparticles; in addition to optimal optical, magnetic, and electrochemical properties, they have a strong chemical reactivity.⁵ Currently, the development of nano-carriers to deliver drugs and/or nucleic acids with or without diagnostic purposes is very promising.^{6–8} Nevertheless, studies to characterize the properties and potential cytotoxic effects of plane nanoparticles are needed to assess their safety in the clinical setting.⁹ Among nanoparticles, nanodiamonds (ND) are of particular interest, because they combine characteristics of nanoparticles with some of the properties of bulk diamond. Their most important characteristics include a high surface/volume ratio, nanometric sizes, maximum hardness and resistance to friction, high thermal conductivity, and chemical stability. These carbon nanocrystals are highly biocompatible. In fact, they remain for long time in the intracellular environment without affecting their molecular mechanisms.^{10,11} Their poor cytotoxicity, even compared with other carbon-based nanomaterials,^{12,13} is proven by their inability to form reactive oxygen species and to induce cell shape changes.¹⁴

Additionally, ND have an intrinsic fluorescence, given by the fluorescent nitrogen vacuum centers, that provide a photostable

Received 6 April 2023; accepted 14 June 2023;
<https://doi.org/10.1016/j.omtn.2023.06.012>.

⁸These authors contributed equally

Correspondence: Prof. Michele Caraglia, Department of Precision Medicine, University of Campania “Luigi Vanvitelli,” Via L. De Crechchio 7, 80138 Naples, Italy.

E-mail: michele.caraglia@unicampania.it

Correspondence: Prof. Silvia Zappavigna, Department of Precision Medicine, University of Campania “Luigi Vanvitelli,” Via L. De Crechchio 7, 80138 Naples, Italy.

E-mail: silvia.zappavigna@unicampania.it



Table 1. Characterization of ND

Formulation	Diameter (nm \pm SD)	Polydispersion index PI \pm SD
ND	56.7 \pm 0.09	0.149 \pm 0.013
ND-PEI	251 \pm 10.3	0.4 \pm 0.05
ND-PEI-miR-34a	304.5 \pm 31.33	0.43 \pm 0.014

Measured values of the mean polydispersion index and hydrodynamic diameter of the samples consisting of ND plain, ND-PEI, and ND-PEI-miR-34a by DLS analysis. All results are expressed as mean \pm SD of at least three independent experiments.

luminescence with near-infrared emission spectra without photo-flashing. In biological applications, ND can also work as optimal monitoring system (Theragnostics).¹⁵

ND have a high conjugability with different molecules such as toxins, proteins, chemotherapy drugs, and nucleic acids (including micro-RNAs) through physical or covalent interactions. Therefore, ND have a greater attractiveness if compared with self-assembling nanoparticles because of their ability to resist changes associated with different biological microenvironments.¹⁰ ND as well as other nanotechnological tools allow the delivery of anti-cancer agents directly in the cancer tissues, often sparing the normal counterparts.¹⁶ This effect is based on the peculiar vascularization of the tumor tissues. In fact, the neo-angiogenesis process is characterized by the formation of fenestrated vessels (differently from those of normal tissues that are irrigated by a continuous endothelium with the exception of some organs such as liver, spleen and lung), thus allowing the passage of nanostructured particles.¹⁷ The presence of the fenestrated vessels with a size from 90 to 150 nm in tumor tissues is perfectly compatible with the dimension of ND that have a mean size of 80–100 nm. Moreover, cancer tissues have a reduced lymphatic drainage. The latter favors the accumulation of the nanocarriers in the tumor, thus concentrating them in proximity of cancer cells. This effect, namely, the enhanced permeability and retention effect, represents the basis of the passive targeting of nanotechnological weapons in tumor site.^{13,18}

MicroRNAs (miRNA) are a class of small non-coding RNAs that negatively regulate the expression of various intracellular targets, playing a key role in the control of cancer growth and spread.^{19,20} MicroRNA-34a (miR-34a) is an oncosuppressor miRNA targeting several signaling molecules involved in multiple tumor progression mechanisms. The well-studied effects of miR-34a on apoptosis and cell-cycle arrest, together with the inhibition of metastatization processes, stemness, and chemoresistance, make miR-34a replacement strategy a possible therapeutic approach against cancer. However, it is necessary to improve the unfavorable biopharmaceutical profile of miRNAs. Indeed, therapeutic strategies involving use of miR-34a as a new anti-tumor agent are limited by the rapid degradation of miRNAs in biological fluids, as well as their low intracellular uptake.^{21,22} These limitations are also paralleled by the so-called off-target effects that can lead to potential toxicities and decreased therapeutic activity. These considerations encourage the development of strategies able to specifically deliver miRNAs in target sites.²³ This

can be achieved by the use of ND conjugated with miRNAs. In the present article, we have designed and developed ND conjugated with miR-34a and we have evaluated the safety and the cytotoxicity of ND-miR-34a on different breast cancer cell lines. We have also studied the transfection efficiency of ND-miR-34a *in vitro* and we have assessed their anti-cancer activity *in vitro* and *in vivo* in both heterotopic and orthotopic breast cancer models.

RESULTS

ND functionalization and characterization

The physico-chemical characterization of ND was performed by measuring polydispersity index, particle size and ζ potential through dynamic light scattering (DLS) analysis. This analysis is based on the measurement of light dynamic diffusion from nanoparticles under the influence of an applied electric field. DLS analysis showed that ND had an average particle diameter equal to 56.7 \pm 0.09 nm and a polydispersity index (PI) of 0.149 \pm 0.013; the complexation of ND with polyethyleneimine (PEI) increased the average diameter (251 \pm 10.3 nm) and the PI (0.4 \pm 0.05), while the addition of miR-34a to ND-PEI did not influence PI (0.43 \pm 0.014) with a slight effect on mean diameter (304.5 \pm 31.33 nm) (Table 1). To study the morphology and dispersity of this delivery system, we performed SEM analysis and observed that ND had always a sub-globular aspect even at higher magnifications (40 kx). Measured dimensions, on a statistically significant number of points, were homogeneous and fell in the range of 20–65 nm (Figure S1 and supplemental methods S1).

Thereafter, we analyzed the surface charge of ND alone or combined with PEI and miR-34a. In detail, the degree of electrostatic repulsion between the adjacent particles in dispersion was evaluated by the migration of the nanoparticles toward the opposite charged electrode with a speed proportional to the amount of charge.

The ζ potential of ND was negative (-22.8 ± 2.08 , mV \pm SD); however, when these nanoparticles were coated with PEI, they became positive ($+16.5 \pm 7.4$, mV \pm SD). Therefore, the addition of PEI played a key role to achieve the interaction between ND and the polyanionic charged miR-34a. In fact, after the binding of the ND-PEI with the miR-34a the negative ζ potential was restored, with a ζ value equal to -26.4 ± 2.50 mV (Figure S2). MiR-34a loading efficiency in ND was additionally confirmed by agarose gel electrophoresis (data not shown); indeed, we found that only ND-PEI-miR34a migrated toward the positive electrode compared with ND-PEI.

Evaluation of ND cytotoxicity and analysis of miR-34a expression by real-time PCR

To evaluate the cytotoxicity of ND without loaded miRNA, we treated breast tumor cell lines using ND-PEI complexes and evaluated the lactate dehydrogenase (LDH) release from cells. The release of the ubiquitous cytosolic enzyme LDH is commonly used to assess cell viability, because it is an index of plasma membrane damage. In detail, after treatment of MDA-MB-231 and MCF7 breast cancer cell lines with ND-PEI for 7, 10, 14, and 17 days, LDH release in cell medium was evaluated using a spectrophotometric assay. Positive (lysed cells)

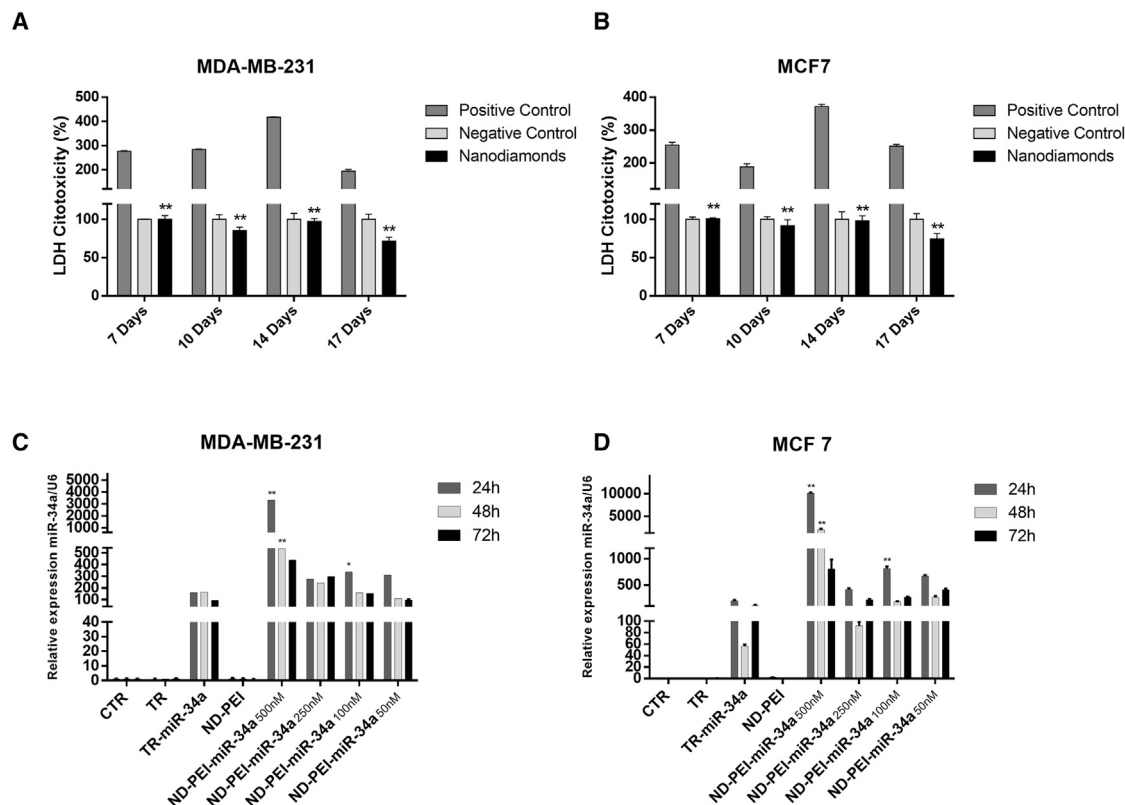


Figure 1. Analysis of cytotoxicity by evaluating LDH release induced by plain ND and Expression of miR-34a in breast cancer cell lines assessed by real-time PCR

Bars, cytotoxicity of nanoparticles in the MDA-MB-231 (A) and MCF7 (B) cell lines was assessed after treatment for 7, 10, 14, and 17 days, with ND treatment every 3 days. (C and D) Delivery to MDA-MB-231 and MCF7 mediated by both the transfectant agent Lipofectamine 2000 and ND conjugated with different concentrations of miR-34a, 500, 250, 100, and 50 nM, respectively, was reported. Each experiment was repeated at least three times and data are shown as mean \pm SD. The samples were statistically analyzed against positive controls in LDH assays and against untreated controls for real-time PCR. * $p \leq 0.05$, ** $p \leq 0.01$.

and negative (untreated normal cells) controls were also included. Figures 1A and 1B show that treatment with ND did not generate any significant cytotoxic effects even at longer times; in fact, LDH release was comparable with those of negative controls.

Subsequently, we have detected the intracellular levels of miR-34a using quantitative RT-PCR to understand if ND-PEI-miR-34a were able to induce intracellular miRNA accumulation useful for replacement strategies.

In detail, we treated breast cancer cell lines with ND conjugated to different concentrations of miR-34a. After 24, 48, and 72 h of incubation with ND or the commercial transfectant agent lipofectamine (TR) used to transfect miR-34a, we observed, in both the assessed cell lines, a significant increase of miR-34a expression. In particular, after 24 h, miR-34a levels were approximately 20-fold and 50-fold higher in MDA-MB-231 and MCF7 treated with 500 nM ND-PEI-miR-34a, respectively, than in conventionally transfected cells (TR, lipofectamine). Also, treatment with 100 nM ND-PEI-miR-34a increased miR-34a expression in MDA-MB-231 (3-fold) and MCF7 (8-fold)

already after 24 h compared with standard lipofection. MiR-34a levels slowly decreased after 48 and 72 h (Figures 1C and 1D).

Analysis of intracellular localization of ND

Interestingly, ND exhibit an intrinsic red fluorescence (633-nm wavelength) that allows us to easily study their intracellular uptake and localization. The red fluorescence associated with the cells transfected with ND was evaluated by fluorescence-activated cell sorting (FACS) analysis after 24 h incubation. In detail, in both cell lines (MCF7 and MDA-MB-231), after 24 h incubation with ND, the percent of mean fluorescence intensity (MFI) detected by FACS was compared with that one of ND in the culture medium (Figure 2A). MFI of untreated cells was assumed as 0%, while MFI of ND in the medium was considered as 100%. In both cell lines, we observed a high internalization of NDs, with an uptake near 100%, but at a major extent in MCF7 cells (83.51% MFI for MCF7 vs. 73.10% MFI for MDA-MB-231) (Figures 2B and 2C).

Moreover, we performed fluorescence microscopy analysis to study the intracellular distribution of ND conjugated with miR-34a after

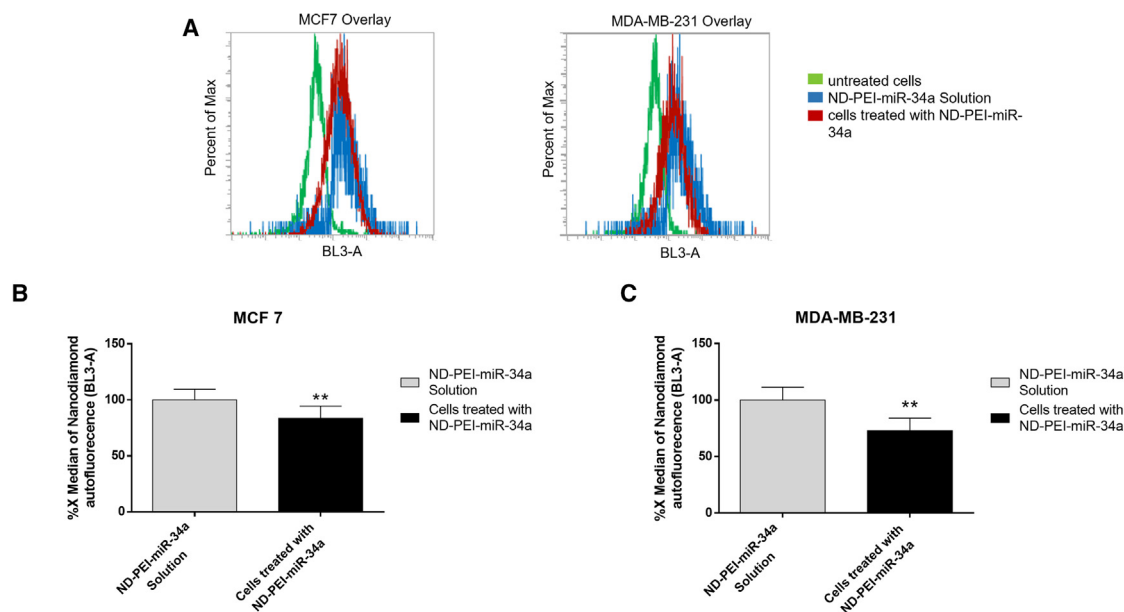


Figure 2. Cell uptake of ND in breast cancer cell lines assessed by FACS

Graphical representation of peaks obtained from cell uptake of ND by flow cytometry in MCF7 and MDA-MB-231 cells after 24 h incubation with ND-PEI-miR-34a evaluated at the absorption peak (BL3 channel-633nm wave-length) (A). Bar graph of the fluorescence emission of ND-PEI-miRNA in solution and in MCF7 (B) and MDA-MB-231 (C) breast cancer cell lines. Each experiment was repeated at least three times and data are shown as mean \pm SD. * $p \leq 0.05$, ** $p \leq 0.01$ (ND-PEI-miR solution vs. cells treated with ND-PEI-miR).

2, 6, and 24 h of incubation. In detail, ND exhibited an intense red fluorescence, the cell nuclei were stained with DAPI (blue) and cytoplasm with FITC-conjugated antibodies against actin (green). Fluorescence images were collected at different times to investigate the progressive accumulation and localization of ND inside MCF7 (Figures 3A, 3B, and 3E) and MDA-MB-231 cells (Figures 3C, 3D, and 3F). Already after 2 h of treatment, red dots associated with ND were visible in the cytoplasm of both breast cancer cell lines. These results confirmed the rapid cell uptake of carbon nanocrystals. Furthermore ND, both uncoated or conjugated with miR-34a, showed a diffuse perinuclear localization, with a progressive increase of internalization over time (Figure 3).

Tumorigenic potential in breast cancer cell lines and cell death processes induced by ND-PEI-miR-34a treatment

To study the antitumor effects of ND conjugated with miR-34a, a colony formation assay was performed on MCF7 and MDA-MB-231 cell lines treated with ND, conjugated to either a random oligonucleotide sequence (NC) or miR-34a. Cells were plated at a very low density and kept in culture for no more than 2 weeks to allow the formation of colonies. Samples were fixed in 70% ethanol and subsequently the colonies were stained with crystal violet and analyzed by ImageJ software. The tumor suppressive activity of miR-34a was evident on the formation of colony-forming units in both MCF7 and MDA-MB-231 cell lines compared with untreated controls, proving its ability to inhibit the tumorigenic potential of breast cancer cell lines. The biocompatibility of ND-PEI without loaded miRNA

was confirmed, as no cytotoxicity was recorded; on the contrary, we found an approximately 50% increase of colony formation as compared with untreated controls. Moreover, we observed a clonogenic rate inhibition of approximately 94% and 64% in MCF7 cells exposed to 100 nM ND-PEI-miR-34a and 500 nM ND-PEI-miR-34a, respectively (Figures 4A–4D). Moreover, both treatments induced a similar inhibition of clonogenic rate (approximately 50%) in MDA-MB-231 (Figures 4A–4D).

Based on previous results on transfection efficiency, we selected the best combinations of miR-34a and ND to investigate the molecular bases underlying the cell death mechanisms. In detail, MCF7 and MDA-MB-231 cells treated with ND-PEI and ND-PEI-miR-34a were stained with FITC-conjugated annexin V and analyzed by FACS after 48 and 72 h. The results showed that addition of miR-34a-ND induced a significant increase in apoptotic cell death after 72 h (Figures 4E and 4F), although no significant evidence of apoptosis was observed at earlier times (data not shown). In particular, approximately 20% and 14% of the MCF7 cell population underwent to apoptosis after exposure to 100 nM ND-PEI-miR-34a and 500 nM ND-PEI-miR-34a, respectively. For MDA-MB-231 approximately 19% of apoptotic cells was recorded after exposure to both 100 nM ND-PEI-miR-34a and 500 nM ND-PEI-miR-34a (Figures 4E and 4F). In addition, cell viability was also investigated by using the Violet Ratiometric Membrane Asymmetry Probe/Dead Cell Apoptosis Kit, which provides a simple and fast method for the detection of live and dead cells by flow cytometry. We found

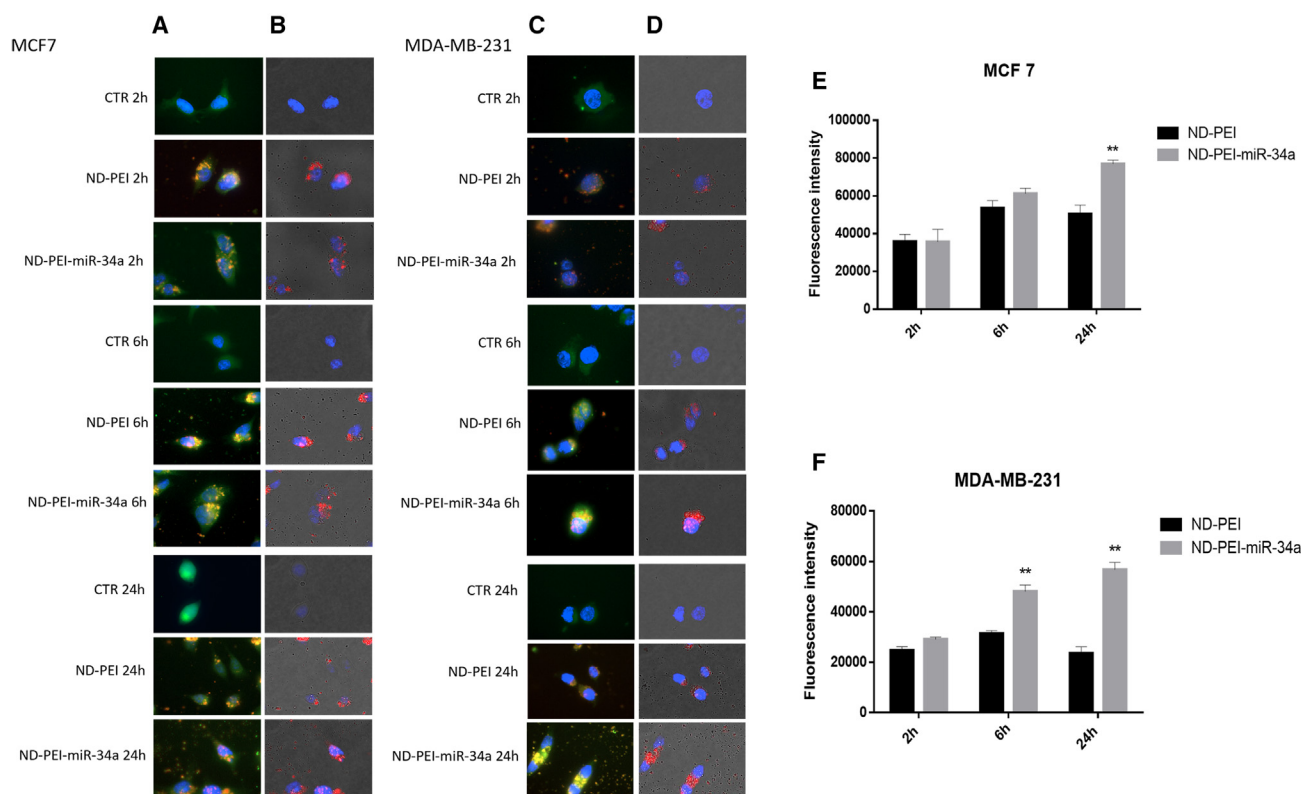


Figure 3. Cell internalization of ND-PEI and ND-PEI-miR-34a in breast cancer cell lines

Intracellular localization of nanoparticles is evident after 2, 6, and 24 h incubation through fluorescence microscopy images (original magnification $\times 100$). Overlay of blue (DAPI, nuclei), red (ND), and green (antibody anti-actin, cytoskeleton) channels in MCF7 (A) and MDA-MB-231 (C) cells. Merge image of brightfield, blue (DAPI, nuclei), and red (ND) channels in MCF7 (B) and MDA-MB-231 (D) cells. Bar graph of the fluorescence emission of ND-PEI and ND-PEI-miRNA in MCF7 (E) and MDA-MB-231 (F) breast cancer cell lines.

that, after 72 h of treatment, 100 nM ND-PEI-miR-34a and 500 nM ND-PEI-miR-34a induced a 2-fold and approximately 1.5-fold increase of dead cell percentage in MCF7 and MDA-MB-231 compared with ND-PEI, respectively (Figure S3 and supplemental methods S.2).

Effects of ND-PEI-miR-34a on cell migration of MCF7 and MDA-MB-231 cell lines

Thereafter, we evaluated the effects of ND-PEI-miR-34a on cell migration through a wound healing assay. The assay was performed evaluating the migration of breast cancer cells after 24 and 48 h of treatment with ND-PEI-miR-34a. In our experimental conditions, we observed the complete repair of the scratch in untreated cells after 48 h. Results obtained on MCF7 and MDA-MB-231 cell lines showed that the inhibitory effect of the ND-PEI-miR-34a on the migration was clearly higher than that one induced after miR-34a lipofection both at 24 and 48 h. The migration rate can be reported as the change in the wound area over time. In particular, 100 nM ND-PEI-miR-34a and 500 nM ND-PEI-miR-34a induced a 69.9% and 30.9% reduction of wound closure (i.e., decrease of migration), respectively, if compared with the untreated MCF7 cells after 48 h from the beginning of the treatment. In contrast, miR-34a lipofection induced

only a 39.8% and 24.8% decrease of cell migration in the same experimental conditions (Figure 5A).

Similar results were obtained in MDA-MB-231 cells. In fact, 100 nM ND-PEI-miR-34a and 500 nM ND-PEI-miR-34a caused an approximately 53.9% and 64.9% decrease in migratory ability detected as percentage of wound area, respectively, if compared with the untreated controls (Figure 5B). Also in this case, the lipofection of miR-34a induced only a 23.9% and 22.9% cell migration decrease in the same experimental conditions (Figure 5B).

In vivo antitumor efficacy and biodistribution of ND-PEI-miR-34a on xenograft heterotopic and orthotopic models of breast cancer

Based on promising *in vitro* results, we performed *in vivo* experiments to evaluate the therapeutic efficacy of ND-PEI-miR-34a. We used two xenograft mice models of breast cancer, one heterotopic, subcutaneously inoculating MCF7 cells in the right flank of the animals, and one orthotopic, injecting MDA-MB-231 LUC cells in the mouse mammary gland. Mice were intravenously treated at a dose of 20 μ g ND-PEI-miR-34a per mouse, and antitumor efficacy was evaluated

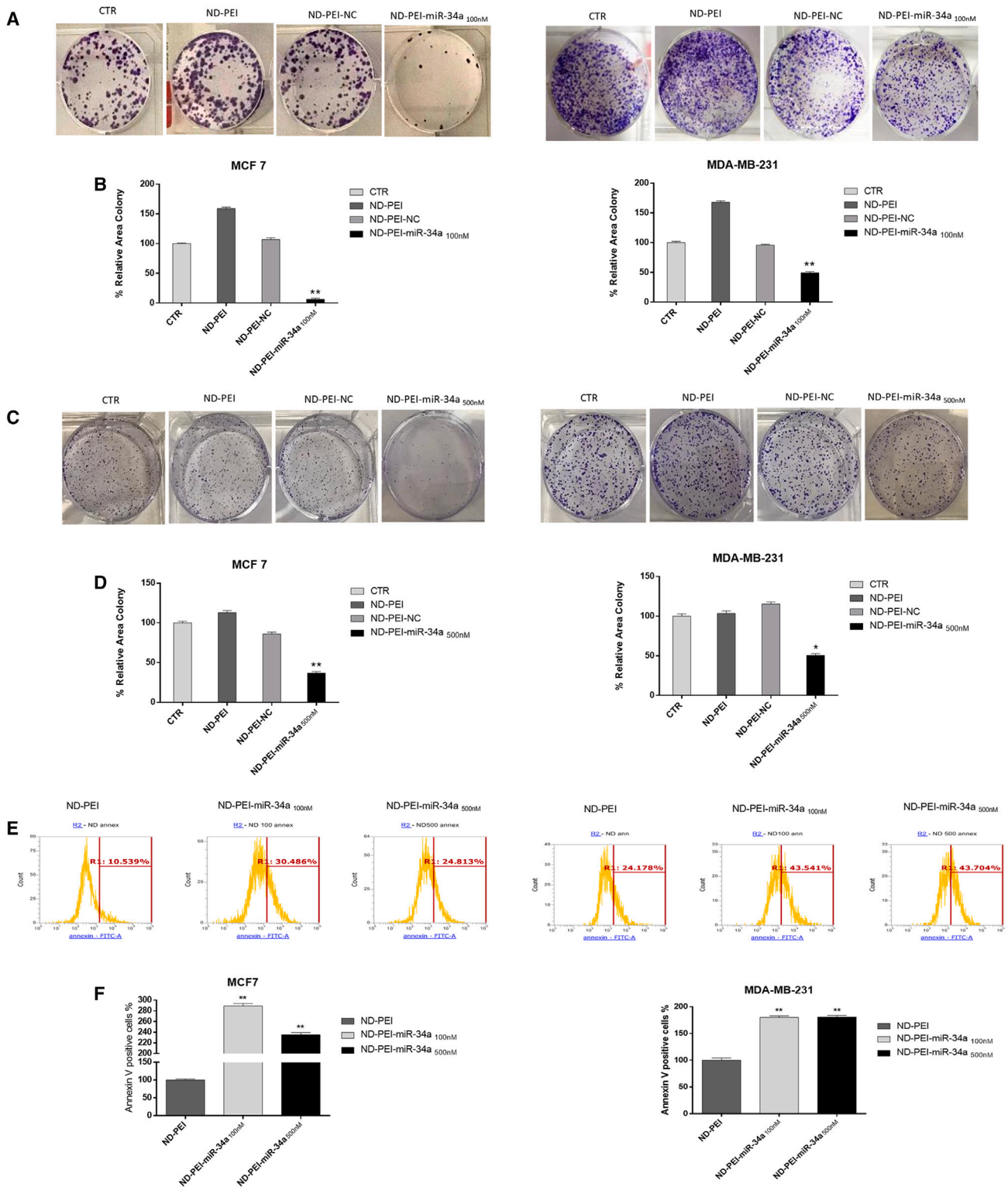


Figure 4. Effects of ND-PEI-miR-34a on tumorigenic potential and apoptosis of cancer cell lines

Different levels of colony formation after treatment with ND-PEI-miR-34a100nM in MCF7 and MDA-MB-231 breast cancer cell lines (A). In detail, the reported samples are untreated control, ND-PEI, ND-PEI-NC, and ND-PEI-miR-34a 100-nM samples. The bars represent the percentage of colony area after treatment for 15 days (B).

(legend continued on next page)

with an *in vivo* imaging system (IVIS) for orthotopic model and a 2BIOL digital caliper for the heterotopic model.

As reported in Figures 6A–6D, we found that treatment with ND-PEI-miR-34a showed a significant antitumor efficacy in both *in vivo* models; moreover, no toxicity (body weight decrease) in heterotopic models was recorded (Figure 6B) and histopathological analysis (Figure S4) of major organs (lungs, liver, kidneys, and brain) excised from orthotopic mouse models showed a normal histological structure.

In heterotopic models, we found a tumor growth inhibition of 57.3% after 24 days of treatment with ND-PEI-miR-34a compared with the inhibition induced by the administration of ND-PEI (only 1.3%) (Figure 6A). In orthotopic models, tumor growth was significantly inhibited during the treatment (23 days) with ND-PEI-miR-34a of approximately 58% compared with an inhibition of photon number of approximately 30% after treatment with ND-PEI. Interestingly, at the end of the treatment (35 days) with ND-PEI-miR-34a, we observed a tumor growth inhibition of approximately 70% compared with the ND-PEI group (Table S1), demonstrating that miR-34a delivered via ND was able to exert a strong antitumor activity *in vivo* (Figures 6C and 6D). Furthermore, we observed a significant increase in the survival of mice treated with ND-PEI-miR-34a compared with untreated mice (Figure S5).

The biodistribution of miR-34a-conjugated ND was investigated in both heterotopic and orthotopic mouse models. In detail, miRNA distribution in brain, lungs, kidneys, spleen, and liver after 4 weeks of treatment with intravenously injected ND-PEI-miR-34a was studied by an RT-PCR technique. Results are reported in Figures 6E and 6F; different levels of miR-34a were detected in the different organs with the highest levels found in the spleen for both models (ND-PEI-miR-34a fold-change [FC]: 253.41 for MCF7 and FC: 43.64 for MDA-MB-231) and in the lung for MDA-MB-231 (ND-PEI-miR-34a FC: 52.41). Moreover, ND-PEI-miR-34a was able to efficiently deliver miR-34a also in tumor tissues of orthotopic mouse models (Figure S6).

Furthermore, we analyzed the ability of the delivered miR-34a to modulate its targets in tumor tissues by immunohistochemical analysis. Since the miR-34/p53 loop has been reported as a key mediator of tumor suppression, we evaluated p53 expression in tumor tissues derived from ND-PEI-miR-34a-treated mouse models. Tumor tissues showed a 12% and 20% positivity for p53 expression in heterotopic and orthotopic ND-PEI-miR-34a groups, respectively, compared with the ND-PEI groups (negative for p53) (Figure S7, Tables S2 and S3). The effect of miR-34a on p53 expression levels was also confirmed by western blot in breast cancer cell lines, selected for

in vivo experiments. In fact, after 72 h treatment with 100 nM and 500 nM ND-PEI-miR-34a, we found an increase of the levels of p53 and its acetylated form in MCF7 and less evident in p53 mutant MDA-MB-231 (Figure S8 and supplemental methods S.3).

In silico analyses were performed to study the correlation between miR-34a expression and overall survival (OS) of breast cancer patients. Patients were categorized into different sub-groups based on ER or HER2 status, pathological grade, lymph node status, and endocrine or chemotherapy treatment by using data derived from the TCGA and METABRIC databases. Kaplan-Meier curve analysis displayed high expression of miR-34a as significantly associated with better OS in all the analyzed sub-groups (Figures S9, S10, S11, and S12) ($p \leq 0.05$), except in lymph node-negative sub-groups of breast cancer patients.

DISCUSSION

MiR-34a family has been reported to be involved in a wide variety of cell processes such as differentiation, proliferation, and apoptosis; therefore, it plays a crucial role in several tumors, acting as a tumor suppressor. MicroRNA replacement represents an innovative and possible therapeutic approach in the treatment of cancer by simultaneously modulating several genes involved in distinct signaling pathways related to neoplastic growth.^{24–28} This research is aimed to design and develop a new miR-34a delivery strategy based on the use of innovative nanoparticles called ND.

Properties of ND include a high specific surface, optical transparency, functional groups containing oxygen on the surface, and a chemically inert core.^{29–31} All these features make ND an excellent tool for biomedical applications. The growing interest in their use has raised concerns about their potential environmental pollution and toxic effects.^{32,33} Nevertheless, it was assumed that carbon-based nanostructures were more biocompatible and less toxic than metal- or semiconductor-based nanomaterials. Multiple studies have evaluated the cytotoxicity of nanocarbons; for example, single-walled nanotubes and fullerene C60 provoked a pronounced cytotoxicity in alveolar macrophages³⁴; in contrast, ND particles were found to be non-toxic to lung or neuronal cells.³⁵ It can be hypothesized that the same carbon-based nanoparticles differ in biocompatibility. Our preliminary experiments were based on the characterization of carbon nanocrystals; in detail, we analyzed the PI of colloidal solution and recorded structure homogeneity and hydrodynamic size of less than 100 nm.

However, in addition to the excellent biocompatibility, there are other factors that make ND favorable candidates for applications in nanomedicine. First is the possibility to synthesize both physically and

Identification of the wells as untreated controls, ND-PEI, ND-PEI-NC, and ND-PEI-miR-34a 500nM samples for MCF7 and MDA-MB-231 breast cancer cell lines (C), with corresponding bars for the evaluation of the percentage of colony area (D). MCF7 and MDA-MB-231 were treated with ND-PEI and ND-PEI-miR-34a for 72 h at concentrations of 100 nM and 500 nM. Early apoptosis was assessed by FACS analysis after labeling with FITC-conjugated annexin V, evidenced by fluorescence peaks with emission in the green channel (BL1 channel) (E). (F) Bars of cells undergoing early apoptosis after treatment with the conjugated nanoparticles in MCF7 and MDA-MB-231. The experiments were performed at least three times and the results were always similar. Data are shown as mean \pm SD. Statistical analysis was performed on the samples by comparing CTR with the treated samples and ND-PEI with the treated samples, respectively. * $p \leq 0.05$, ** $p \leq 0.01$.

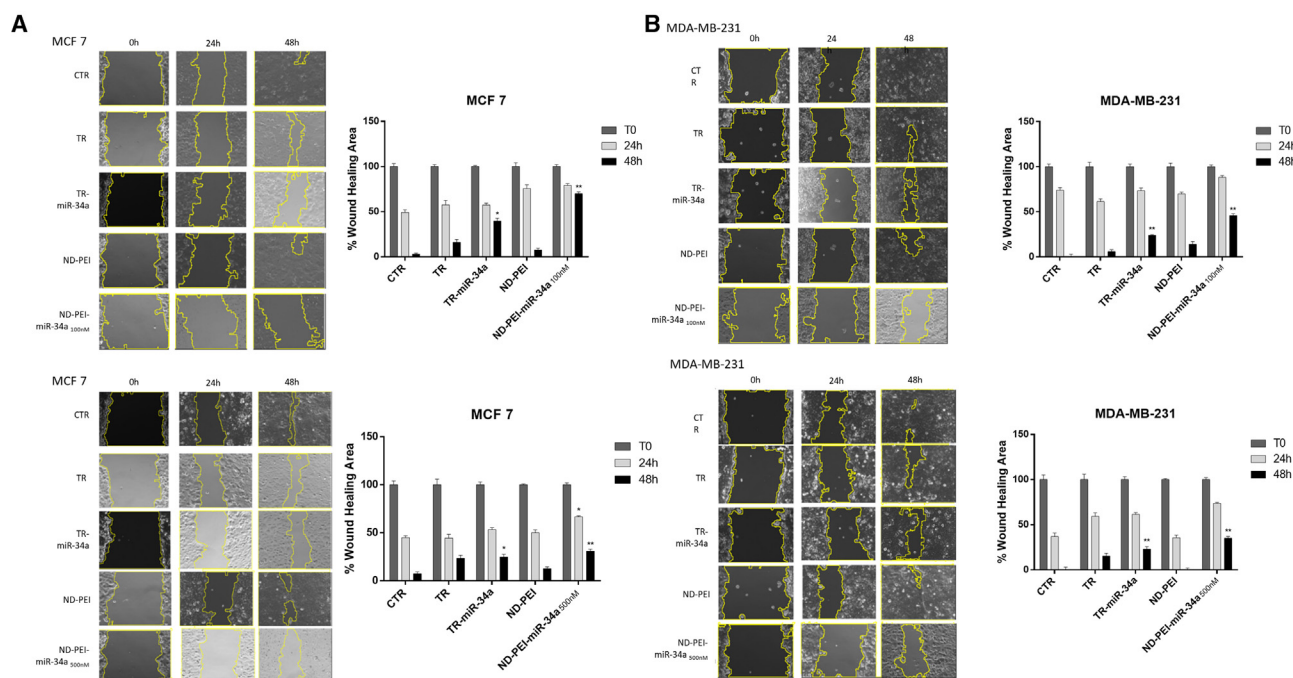


Figure 5. Effects of miR-34 on Migration of MCF7 and MDA-MB-231 Cells

Confluent monolayer of breast cancer cells, transduced with miR-34 by conventional transfectant or treated with ND-PEI-miR-34a, were scratched to create an artificial wound viewed by microscopy (original magnification $\times 20$). (A) miR-34a mimic effects on cell migratory ability was recorded by microscopy at T0 and after 24 and 48 h and analyzed in comparison with untreated controls (CTR), quantitated with ImageJ. (B) MDA-MB-231 cells transduced with miR-34a were assayed in comparison to CTR. Error bars show mean \pm SD. * $p \leq 0.05$, ** $p \leq 0.01$.

chemically carbon nanocrystals^{36,37}; these carbon allotropes also show high rigidity and low chemical reactivity.³⁸ Furthermore, oxygen-containing groups on the surface of ND allow their functionalization with biomolecules or drugs by physical or chemical methods. On these bases, to develop a new miRNA delivery system based on ND, we studied the surface charge of ND by ζ potential analysis. Because of the dissociation of surface groups containing oxygen in aqueous phase, ND show a negative ζ potential ranging from -30 meV to -50 meV. Therefore, molecules with a positive polarity (typically amino groups) can be absorbed through an electrostatic interaction on ND surface. The addition of polymers on the surface of ND allows a range of different functionalization strategies.³⁹ In our case, we would optimize the functionalization of ND with miR-34a; because of the negative charge of ND, it was required to form a bridge between the nanoparticles and the polyanionic nucleic acid. Multiple studies reported PEI as one of most extensively used cationic polymers in interacting with nucleic acids. On these bases, we selected PEI as the linker between ND and miR-34a.^{40,41} However, two PEI coating layers were found to be less effective and more toxic than the combination of PEI and a degradable polymer.⁴² The values of ζ potential that we obtained from Zetasizer demonstrated the adequate PEI coating on the surface of ND and the correct binding with miRNA molecules. Indeed, from our data it was clear that ND were successfully coated with PEI800 because they showed a positive ζ value. Positivity of ND-PEI complex is caused by the interaction

between the oxidized ND surface and PEI and plays a key role to bind miRNA molecules. In contrast, ND conjugated with miR-34a had a negative ζ potential, suggesting the correct connection of miR-34a molecules on ND surface. Delivery of nucleic acids based on nanotechnologies allows us to protect them from enzymatic degradation and to prolong their circulation time after intravenous administration.^{42–44}

The lower cytotoxicity of ND compared with other nanocarbons and with other vector systems is of paramount interest.^{13,45} The biocompatibility of ND-PEI was assessed by lactic dehydrogenase assay. From *in vitro* experiments, we did not record any cytotoxicity, even after long periods of treatment in all cell models of breast cancer. Additional studies aimed to analyze the internalization efficiency of ND in MCF7 and MDA-MB-231 cell lines. Therefore, we performed real-time PCR to evaluate the delivery mediated by the diamond nanocrystals in comparison with the commercial transfectant. MiR-34a delivered by ND was significantly higher than that provided by conventional lipofection in both cell models. Moreover, this analysis allowed us to select the best ND-PEI-miR-34a combinations for the subsequent functional assays. In detail, for breast carcinoma models, the formulations 500 nM ND-PEI-miR-34a and 100 nM ND-PEI-miR-34a were selected. Another interesting property of ND is their intrinsic fluorescence, useful to investigate their cellular uptake. In fact, FACS analysis showed that ND almost completely accumulate

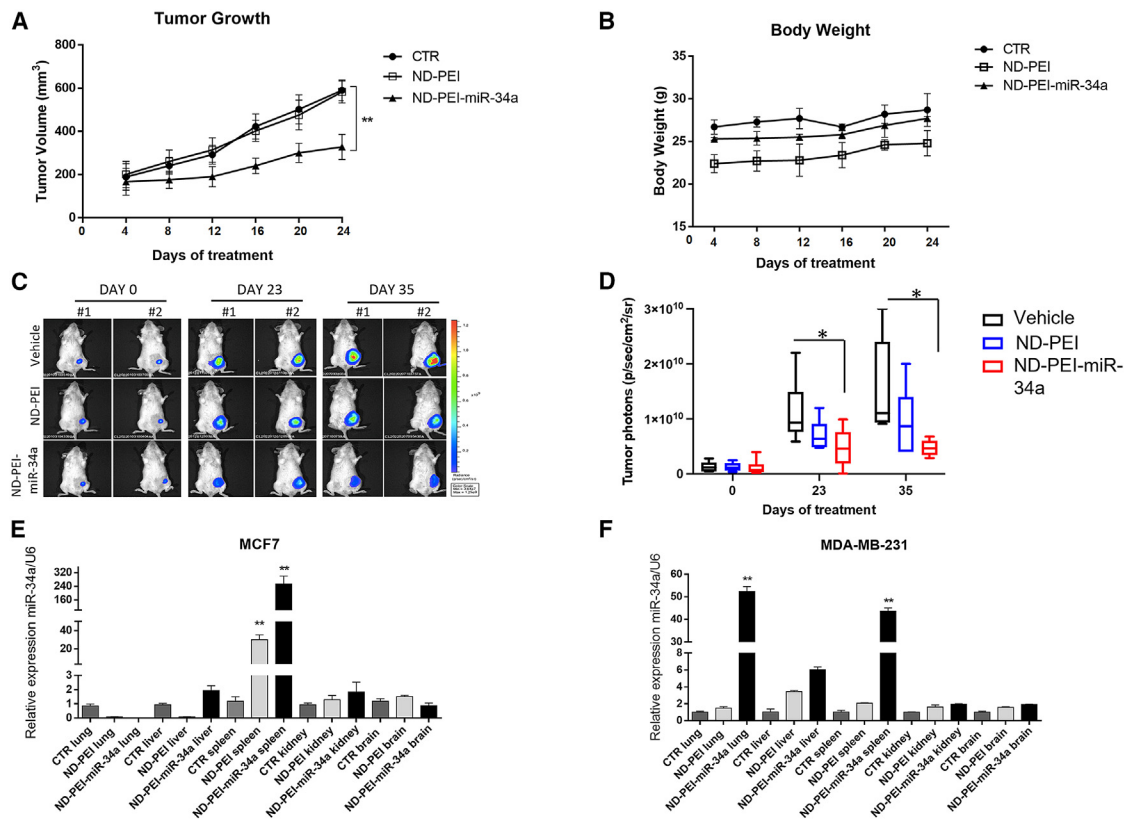


Figure 6. Effects of ND-PEI-miR-34a on orthotopic and heterotopic xenograft mouse breast cancer models and evaluation of miR-34a levels in brain, lungs, kidneys, spleen, and liver

(A) Mice were randomized into three groups (each group n = 8 mouse) and treated intravenously (iv) with vehicle, ND-PEI, and ND-PEI-miR-34a at 20 μg/mice twice a week for 4 weeks. MCF7 was inoculated into the CD-1 nude mice and, when the tumors reached a mass of approximately 200 mm³, the treatments were started. Tumor growth was followed by caliber measurements (A). (B) Tumor weight in untreated mice or mice treated with ND-PEI plain and ND-PEI-miRNA was reported at the nadir of the effect. (C) Anti-tumor efficacy of the ND formulations was also evaluated in an orthotopic xenograft model of mammary carcinoma by inoculation of MDA-MB-231 cell line in female NOD SCID mice. Real-time tumor growth was monitored with the IVIS Lumina II CCD camera system (PerkinElmer). Representative pictures (mouse #1 and mouse #2) (C) of *in vivo* bioluminescence imaging analyzed before administration of compounds (day 0), during the treatments at days 23 and at the end at day 35. Quantitative analysis (D) of *in vivo* luciferase activity at different time points. Data were acquired and analyzed using the Living Image Software version 4.3 (PerkinElmer). The luminescent signals are expressed as mean ± SD of the total photon flux/s/cm²/steradian (p/s/cm²/sr). Data were analyzed by t test (*p = 0.04 [day 23]; *p = 0.01 [day 35]; n = 8). (E) Subcutaneous tumor xenotransplantation model for breast cancer in mice CD-1 nude with relative expression of miR-34a levels accumulated in brain, lungs, kidneys, spleen, and liver represented by bars. (F) Expression of miR-34 in organs selected for the orthotopic NOD SCID model of tumor xenotransplantation. Statistical analysis was performed on the samples compared with untreated controls. *p ≤ 0.05, **p ≤ 0.01.

inside the cells after 24 h and these data were confirmed by fluorescence microscopy. In detail, we analyzed the intracellular distribution of ND by fluorescence microscopy; they showed a widespread perinuclear and nuclear localization in breast cancer cell lines. Cellular accumulation was already evident after 2 h and progressively increased over time. These results are in line with the literature; it is reported that the internalization of ND through endocytosis has been proven in various cell lines, including normal human HFL-1 fibroblasts and A549 human lung adenocarcinoma cells.^{46,47} Studies performed by Faklaris et al.⁴⁸ demonstrated that ND with a size of approximately 46 nm are internalized in HeLa cells, mainly through clathrin-mediated endocytosis, and a perinuclear and nuclear localization of ND can be observed in HeLa cells after 2 h of incubation. Recently, it was shown that only a modest number of ND enter through the endo-

cytosis pathway; in fact, fluorescent ND can be also internalized via endolysosomes and finally excreted from the cells.⁴⁹ We have performed clonogenic and wound healing assays to verify the anti-cancer efficacy of our strategy. Colony analysis after treatment with ND-PEI-miR-34a showed a decrease in the tumorigenic potential of breast cancer cell lines if compared with the controls. In detail, 100 nM ND-PEI-miR-34a gave better results in MCF7 cells if compared with those treated with a higher miR-34a concentration. The MDA-MB-231 cell line showed similar results with both ND-PEI-miR-34a concentrations. Moreover, both 100 nM and 500 nM ND-PEI-miR-34a similarly inhibited cell migration of MDA-MB-231, while the best anti-migratory effect on MCF7 was recorded with 100 nM ND-PEI-miR-34a. Our data confirmed that the reintroduction of miR-34, poorly expressed in various tumor tissues,

downregulates tumor growth both *in vitro*^{21,50} and *in vivo*. The biodistribution of miR-34a delivered by ND has been studied in two xenograft mice models of breast cancer. Different levels of miR-34a were detected in the various organs, with the highest levels found in the spleen for both models and in the lung for the orthotopic model. Similar results were also obtained by the research group of Yuan et al.⁵¹; in fact, they showed that intravenously injected ND predominantly accumulated in liver, lungs, and spleen of murine models. The biodistribution of nanovectors depends on their properties and interactions throughout the body; for example, size can affect the biodistribution of nanoparticles. Generally, larger nanovectors accumulate in the liver and spleen because of macrophage uptake.⁵² However, we found that miR-34a delivered through ND exerted a strong *in vivo* antitumor effect by reducing tumor growth of more than 50% in an orthotopic triple-negative breast cancer model. Moreover, we recorded a modulation of miR-34a targets (p53 and its acetylated isoform) in tumor tissues as evaluated by immunohistochemistry and western blot, thus suggesting that ND were able to successfully deliver miR-34a.

Our results showed that ND-PEI-miR-34a were able to induce growth inhibition and apoptosis in both cell models MCF7 (wild-type p53) and MDA-MB-231 (mutant p53). MiR-34a is part of a positive regulatory loop acting on p53 and together with sirtuin 1 (SIRT1) plays a key role in regulating p53 post-translational modifications and its transcriptional activity. Recent studies have shown that miR-34a is able to promote apoptosis rather than autophagy by downregulating multiple targets, including SIRT1.⁵³ SIRT1 inhibition leads to an increase of acetylated p53 expression together with the p53 transcriptional targets, p21 and PUMA, that play a key role in cell cycle and apoptosis, respectively. In line with other studies,⁵⁴ Chakraborty et al.⁵⁵ identified AMP-activated protein kinase (AMPK) and SIRT1 as key molecular players in a regulatory loop that enhanced autophagy mediated by nitrosative stress in MCF7. They suggested that the AMPK-SIRT1 axis could affect p53 transcriptional activity through deacetylation to induce autophagy, but not apoptosis.⁵⁵ Moreover, an additional study found that either AMPK or SIRT1 inhibition by using siRNA treatment increased the acetylated form of p53, thus inducing the transcription of pro-apoptosis genes in the stress response.⁵⁶ Autophagy and apoptosis are strictly interconnected. When caspases are activated, beclin-1 decreases and leads to the inhibition of autophagic flux.⁵⁷ Liao et al.⁵⁸ found that the overexpression of miR-34a led to the inhibition of autophagy-related proteins, ATG4B, beclin-1, and LC3B II/I. In contrast, decreased miRNA-34a expression is correlated with greater cell growth, apoptosis inhibition, and autophagy activation through the AMPK/mammalian target of rapamycin pathway regulation in prostate cancer.⁵⁸ We found that ND-PEI-miR-34 induced the accumulation of acetylated p53 in tumor tissues of MCF7 xenograft mouse models, thereby inhibiting tumor growth and overcoming the effect of beclin 1 and caspase 3 deficiency. In agreement with other studies,^{53,59} we found that miR-34a overexpression decreased cell proliferation and increased p53 expression even in p53 mutant MDA-MB-231. Indeed, Cao et al.⁵⁹ reported that the acetylation of p53 at Lys382 induced by

ACY1215 partially restored mutant p53 to its normal conformation in MDA-MB-231 cells. In addition to the inhibitory role of SIRT1 on p53 transcriptional activity, it is also involved in Rb deacetylation, thereby inducing cell-cycle progression.⁶⁰ Hence, through Rb pathways, SIRT1 down regulation may induce cell-cycle arrest and apoptosis in p53 mutant cells as well.

Recently, miRNA-based therapeutics, including miR-34 mimics, passed from the bench to the bedside with promising results in the treatment of several diseases, but inducing unexpected side effects as well (hyperactivation of the immune system causing also treatment-related deaths). These results strongly support the design and development of strategies to specifically deliver miRNAs in the diseased tissues, sparing the normal counterparts and thus avoiding the so-called off-target effects of miRNAs. Our results suggest that ND-based delivery systems seem to be a promising strategy to replace miR-34a in cancer tissues to achieve safe and effective targeting of cancer. Active targeting with cancer-specific molecules could additionally improve ND biodistribution by decreasing their uptake by MPS and increasing accumulation in tumor sites.

Conclusions

Our scientific goal was to investigate the efficiency of a novel ND-based system to deliver miR-34a, a known tumor suppressor miRNA, to breast cancer tissues. We have prepared PEI-coated ND to develop positively charged complexes able to bind miR-34a. The ability of the PEI coating to bind miRNA was demonstrated by measuring the ζ potential changes of each complex. We performed LDH release assay of cells treated with ND-PEI complexes, confirming their biocompatibility in all the examined models. *In vitro* experiments on MCF7 and MDA-MB-231 cell lines were performed to evaluate the delivery of miR-34a with ND-PEI complexes compared with conventional lipofectamine. In detail, real-time PCR showed a very significant increase in miR-34a levels in all cell lines treated with ND-PEI-miR-34a if compared with the commercial transfectant. We confirmed cellular internalization by fluorescence microscopy and cytofluorimetry analysis using the intrinsic labeling of ND. Experimental data obtained from cell survival assays demonstrated the advantageous efficiency of ND combined with miR-34a as delivery system. These encouraging results were paralleled by the strong anti-cancer *in vivo* activity of ND-PEI-miR-34a in both heterotopic and orthotopic murine breast cancer models. In conclusion, the development of an *ad hoc* delivery system to deliver miR-34a has been proven to be an innovative and efficient therapeutic approach, pointing toward the transition from basic research to clinical trials.

MATERIALS AND METHODS

Preparation of ND complexes

ND were purchased from Adámas Nanotechnologies and functionalized in collaboration with the Department of Biophysics at Charles University in Prague. In detail, carboxylated 40 nm red fluorescent ND were diluted in distilled water, ≤ 1.5 ppm NV FND 10 mL (NDNV40nmHi10ml) with a final concentration of 1 mg/mL. To create a coating of positively charged ND to obtain an electrostatic

bond with miRNA, we used PEI (Sigma-Aldrich). Before use, ND were dissolved in water and sonicated with a probe for 45 min. The resulting transparent colloid was filtered using a 0.2 μm PVDF micro-filter. ND diluted in water were coated with 0.09 mg/mL PEI 800, adding the same volume of both solutions. Then the mixture was swirled overnight to allow the PEI molecules to adhere to the ND. The next morning, the resulting suspension with ND-PEI complexes and free PEI molecules was centrifugated at $13,400\times g$ for 30 min to create ND-PEI pellets on the bottom of the microcentrifuge tube eliminating supernatant with the free PEI molecules. This pellet was diluted in water free of RNase/DNase. ND easily aggregate and thus create clusters. Clusters have been disaggregated by ultra-sonication in a sonic bath, as the bound energy causes agitation of clustered particles by breaking them up. With a view to generate the link between miRNA and ND-PEI, ND-PEI have been mixed with the miRNA for 1 h at room temperature.

ζ Potential analysis

For the analysis of the ζ potential, we used Malvern's Zetasizer Nano Z at the Department of Pharmacy of the University Federico II of Naples. The ζ potential was measured by the Laser Doppler micro-electrophoresis, which applies the electric field to a solution and the particles in solution move with a speed related to their ζ potential.

This analysis allowed the determination of polydispersion index and hydrodynamic diameter of ND providing also information on the electrostatic charge of the different colloidal suspensions.

The samples analyzed were as follows:

- ND: 15 μL of 1 mg/mL ND + 585 μL of RNase/DNase free water.
- ND-PEI: 15 μL of 1 mg/mL ND-PEI + 585 μL of RNase/DNase free water.
- ND-PEI-miR-34a: 15 μL of 1 mg/mL ND-PEI-miRNA-34a + 585 μL of RNase/DNase free water.

Fifteen microliters of volume in 600 μL of H_2O provided the best results for ζ potential measurement.

When the speed of variations in intensity of diffused light and particle diffusion coefficient calculated by correlation function are measured as a function of time, information is obtained regarding the hydrodynamic diameter and the state of aggregation of colloidal solution. At the same temperature and viscosity, small particles move rapidly, creating rapid variations in the scattering intensity, while large particles moving slowly.

Cell cultures

Our experimental system is represented by cell lines derived from human breast carcinoma MCF7 and MDA-MB-231, which were purchased by the American Type Culture Collection. MDA-MB-231 cells were cultured at 37°C in a 5% CO_2 atmosphere in RPMI 1640 medium containing L-glutamine (Gibco, Life Technologies) with the addition of 10% fetal bovine serum (FBS) heat inactivated at 56°C for

20 min (Lonza Group Ltd) and 1% of a solution of penicillin and streptomycin (Gibco, Life Technologies). MCF-7 cells were grown at 37°C in a 5% CO_2 atmosphere, in a DMEM medium (Gibco, Life Technologies), with the addition of 10% FBS heat inactivated at 56°C for 20 min (Lonza Group Ltd), 1% L-glutamine and 1% penicillin and streptomycin (Gibco, Life Technologies). For *in vivo* experiments, MDA-MB-231 were infected with lentiviral luciferase vector pRRLSIN.cPPT.RFPL4b.Luciferase (Addgene) (MDA-MB-231 LUC).

LDH assay

LDH assay is a colorimetric assay used for the quantitative assessment of cellular cytotoxicity. LDH is an enzyme released from damaged cells in growth media. The cells release many enzymes after their death, but to detect the activity of the enzyme in the culture supernatant it must have some characteristics: because of the reproducibility of the test, it must be stable, resistant to decomposition by proteases, and expressed in a sufficient amount in the target cells. LDH has all these characteristics. LDH catalyzes the oxidation of lactate to pyruvate and the reduction of NAD^+ in NADH and H^+ . This enzymatic activity can be detected and quantified with another enzymatic reaction. The tetrazolium 2-(4-iodophenyl)-3-(4-nitrophenyl)-5-phenyl-2H-tetrazolium chloride salt is reduced to formazan salt using the diaphorase enzyme as a catalyst. Formazan has a maximum absorption of approximately 500 nm.⁶¹ This stained product can be detected by the spectrophotometer able to read the required wavelengths. The cells were seeded in 96-well plates (800 cells per well) and subsequently treated with different concentrations of ND-PEI. After different times of incubation, the analysis was performed to evaluate LDH activity using Cytotoxicity Detection KitPLUS from Roche. The absorbance of the supernatants was measured at a wavelength of 490 nm on the iMark Microplate Absorbance Reader (BioRad). LDH activity measurement was normalized compared with a positive control with maximum release of LDH and a basal release from untreated cells. These experiments were performed in triplicate.

In vitro transfection of cancer cell lines

MCF7 and MDA-MB-231 breast cancer cell lines were seeded at a density of 2.1×10^3 cells per well in 96 multi-well plates. Mimic miR-34a and the negative control represented by a scrambled sequence of the oligonucleotide (NC) were purchased from Life Technologies. For a comparison of intracellular miRNA delivery by ND, we used lipofectamine 2000 (ThermoFisher Scientific), a well-known reagent used for transfection. Commercially available transfectant agent is used to release DNA and RNA molecules into the cells, because of the head group loaded with cationic lipids that can provide transport across cell membrane. The transfection reagent was mixed with miRNA, following the protocol provided by the manufacturer. After cell seeding (approximately 3–4 h), medium was replaced with starvation medium with 1% FBS. Cells were incubated in starvation medium overnight and then exposed to the stimulation mixture that includes either ND-PEI complexes or lipofectamine with miRNA.

Real-time qPCR

Total RNA was extracted from either breast cancer cell lines or mouse tumors using mirVana miRNA Isolation Kit (Life Technologies) according to the manufacturer's instructions. Subsequently, the integrity, quality and quantity of RNA were evaluated by NanoDrop ND-1000 spectrophotometer (ThermoFisher Scientific).

Oligo-dT-primed cDNA was obtained using the High Capacity cDNA Reverse Transcription Kit (Applied Biosystems). The single-tube TaqMan miRNA assays (Ambion, Life Technologies) were used to detect and to quantify mature miR-34a, according to the manufacturer's instructions by real-time PCR Viia7 TM (Applied Biosystems). MiR-34a expression was normalized by the housekeeping U6 (Ambion, Life Technologies). Comparative real-time PCR was performed in triplicate, including no template controls, and relative expression was calculated using the comparative cross-threshold method.

Evaluation of ND internalization through FACS analysis and fluorescence microscopy

The analysis of the intracellular distribution of ND was carried out by both FACS and fluorescence microscopy. ND were incubated with MCF7 and MDA-MB-231 cells for a variable time (2, 6, or 24 h) at 37°C. Attune NxT Flow Cytometer (Invitrogen) was used to perform flow cytometry analysis of ND intracellular distribution. ND is a bright, red fluorescent dye with excitation and emission wave-lengths similar to PE. After incubation with ND at 37°C, removal of not encapsulated ND was accomplished by washing the cells with PBS at a pH of 7.4 for 1 min. Thereafter, cells were detached by trypsinization. The samples were subsequently washed twice, and for each sample, 25,000 cells were analyzed through FACS using the Attune Cytometric Software. The MFI of ND directly dissolved in the medium was considered as 100%.

After 2, 6, or 24 h of incubation with ND, MCF7 and MDA-MB-231 cells were fixed for 15 min with a 4% (w/v) paraformaldehyde solution and permeabilized for 10 min with 0.1% (w/v) of Triton X-100 in PBS at room temperature. To prevent the development of non-specific antibody interactions, the cells were treated for 1 h with a 5% FBS/PBS solution and, finally, the cells were incubated with monoclonal specific anti β -actin mouse monoclonal antibody conjugated to Alexa Fluor 488 (1:1000 in blocking solution) overnight at 4°C in agitation. The slides were mounted with a mounting medium, Moviol containing DAPI (ProLong Diamond DAPI, Life Technologies), on slides suitable for oil immersion and evaluated at the microscope at a 100 \times magnification. The analysis was performed with an EVOS XL imaging system microscope (ThermoFisher Scientific).

Wound healing assay

Wound healing is a test developed for the *in vitro* assessment of cell migration. MDA-MB-231 and MCF7 cells were seeded in 24-well plates at a density of 8×10^4 cells/well. After treatment with ND-PEI-miR-34a, a scratch was created on the cellular monolayer by scraping it with a sterile tip. The cell monolayer was then washed with PBS to remove the floating cells and complete medium was added.

Images (5/field) of the scratched surface were acquired (20 \times magnification) using a microscope EVOS XL imaging systems microscope (ThermoFisher Scientific) immediately after scratching and after 24 and 48 h of incubation. The images of the treated cells were compared with those of control cells to assess the effects of ND-PEI-miR-34a on the cells' ability to repopulate the cell-missing area and the percentage of the closure area was calculated using ImageJ software.

Flow cytometric analysis of apoptosis

MCF7 and MDA-MB-231 cells were transfected in our experimental condition with miR-34a mimic, as previously described. Furthermore, the apoptotic pathway in cells transfected with ND-PEI-miR-34a was also evaluated. Annexin V-FITC (fluorescein isothiocyanate) (BD Pharmingen) was used to discriminate apoptotic cells. After the treatments, cells were collected and centrifuged for 5 min at 1,200 rpm. Pellets were washed in PBS and incubated with annexin-V-FITC in a binding buffer (10 mM HEPES, pH 7.4, 150 mM NaCl, 5 mM KCl, 1 mM MgCl₂, 2.5 mM CaCl₂) for 30 min at room temperature, washed, and re-suspended in PBS as described by the manufacturer. Analysis of apoptotic cells was performed using Attune NxT Flow Cytometer (Invitrogen). For each sample, 2.5×10^4 events were acquired. Analysis was carried out by triplicate determination on at least three separate experiments.

Clonogenic assay

A clonogenic assay was performed to observe the contact-independent growth of breast cancer cells. We seeded 50,000 cells/well in 500 μ L of complete medium with 10% FBS in 24-well plates. The plates were incubated at 37°C, in a humidified atmosphere with 5% CO₂ and we treated or not the cells with ND-PEI-miR-34a as previously described. Subsequently, after 24 h of incubation the cells were detached and seeded in 6-well plates at a density of 1,000 cells/well in 2 mL complete medium with 10% FBS and incubated again at 37°C, in a humidified atmosphere with 5% CO₂ for 15 days with medium change every 3 days. The colonies were fixed with 70% ethanol for 30' and stained with 0.025% crystal violet (Sigma-Aldrich). The visible cellular colonies were counted by ImageJ software.

In vivo study

Heterotopic xenograft model was generated with 6-week-old female CD-1 nude mice into which MCF7 (1×10^6) were injected via an insulin syringe with a 27G nest. To ensure and maintain tumor growth in the heterotopic model, inoculated animals will be administered a dose of estradiol at 6.25 μ g/mL in water supplied ad libitum. Tumor growth for the heterotopic model was measured every 2–3 days with a 2BIOL digital caliper. Mice were housed in specific pathogen-free conditions and maintained in individually ventilated cages under constant conditions of temperature ($22 \pm 2^\circ\text{C}$), humidity ($55\% \pm 10$ UR) and 12-h cycles of light and dark. Mice had free access to irradiated standard diet and water.

The orthotopic model was generated by the injection in the mouse mammary gland of 7-week-old female NOD SCID immunodeficient mice (Charles River Laboratories) of MDA-MB-231 LUC cells

(1×10^6) using an insulin syringe with a 27G needle. Mice were anesthetized with a combination of tiletamine–zolazepam (Telazol) and xylazine (Rompun) given intramuscularly at 2 mg/kg, and a small incision of less than 3 mm is made externally and caudally to the nipple. With the aid of micro-dissecting forceps, the ventral-most part of the fat pad is gently pulled out and exposed through the small incision.⁶² Successful injection is confirmed by the swelling of the tissue. The small incision is sealed using absorbable suture (PolySorb 5-0). Finally, mice were medicated with an oral administration of 0.5 mg/kg meloxicam (Metacam) to control post-operative pain and inflammation. Real-time tumor growth was monitored weekly using the IVIS Lumina II CCD camera system (PerkinElmer) by intraperitoneally injection with 150 mg/kg D-Luciferin (PerkinElmer) for the orthotopic model.

When the tumors were palpable in the orthotopic model and when it reached a tumor volume of approximately 200 mm³ in the heterotopic model, mice were randomized into three groups and treated intravenously with vehicle, ND-PEI, or ND-PEI-miR-34a 20 µg/mice twice a week for 4 weeks. Imaging was performed at baseline and at days 23 and 35 after starting the treatment. Bioluminescence signals were determined by the number of photons and were acquired and analyzed using the Living image software version 4.3 (PerkinElmer).

Tumor growth was evaluated at days 10, 13, 17, 20, and 24 during treatment by caliper and were evaluated as volume in accordance with the formula $V = (a \times b^2)/2$, where a is the largest surface diameter and b the smallest surface diameter. All efforts were made to minimize animal suffering (ARRIVE release 2.0 Checklist in Supplemental Section). Each experimental group included eight mice. At the end of the treatment, two mice per group were sacrificed by euthanasia with carbon dioxide and organs were explanted to perform immunohistochemistry (IHC) and molecular analysis.

Animal procedures were approved by the Italian Ministry of Health (authorization No. 386/2020-PR, released date 30/04/2020) and followed national and international directives (D.L. 4 March 2014, no. 26; directive 2010/63/EU of the European Parliament and of the council; Guide for the Care and Use of Laboratory Animals, United States National Research Council, 2011).

IHC analysis

IHC staining was performed on 4-µm-thick whole sections. IHC assays were performed using the VENTANA antibody anti-p53 (DO-7) and the ultraView kit (Ventana Medical Systems Inc.), as a fully automated assay on the Ventana BenchMark XT processor. The samples were considered positive when tumor cells (any percentage of positive tumor cells) showed a nuclear staining.

Statistical analyses

The statistical analysis was carried out using ANOVA. Significant differences were determined at a p value of ≤ 0.05 , based on the Student's t test. Graphs were obtained using the programs Microsoft Excel, SigmaPlot version 11.0, GraphPad Prism 6, ImageJ software.

DATA AVAILABILITY STATEMENT

Data supporting the figures generated are available from authors under written demand.

SUPPLEMENTAL INFORMATION

Supplemental information can be found online at <https://doi.org/10.1016/j.omtn.2023.06.012>.

ACKNOWLEDGMENTS

This study was supported by the University of Campania L. Vanvitelli through the grant VALERE: Vanvitelli per la Ricerca program GO MAGIC and by Regione Campania through the grant entitled “Basi (EPI)GENetiche virali e dell’ospite di suscettibilità alla infezione da SARS-CoV-2 (acronimo: EPIGENIUS-SARS-CoV-2).” The authors acknowledge Dr Roberto De Gennaro for the assistance with SEM observations and the use of microscopy laboratory of the Department of Earth Sciences, Environment and Resources, University of Naples Federico II.

AUTHOR CONTRIBUTIONS

M.A., A.Lo., S.Z., G.M., and M.C. designed the study; M.A., A.Lo., and M.P. wrote the manuscript. M.A., A.Lo., A.Lu., M.P., R.A., M.B., V.C., S.F.G., V.N., F.Z.M., and A.R. performed data analysis. M.P., C.L., G.D., F.C., R.F., M.S., R.S., R.A., G.M., and E.A. contribute to manuscript revision. M.A., S.Z., and M.C. coordinated and edited the final version of the manuscript for important intellectual content. All authors read and approved the final manuscript.

DECLARATION OF INTERESTS

The all authors declare that they have no conflicts of interests.

REFERENCES

1. Van der Meel, R., Sulheim, E., Shi, Y., Kiessling, F., Mulder, W.J.M., and Lammers, T. (2019). Smart cancer nanomedicine. *Nat. Nanotechnol.* *14*, 1007–1017.
2. Mukherjee, A., Waters, A.K., Kalyan, P., Achrol, A.S., Kesari, S., and Yenugonda, V.M. (2019). Lipid-polymer hybrid nanoparticles as a next-generation drug delivery platform: state of the art, emerging technologies, and perspectives. *Int. J. Nanomed.* *14*, 1937–1952.
3. Markman, J.L., Rekechenetskiy, A., Holler, E., and Ljubimova, J.Y. (2013). Nanomedicine therapeutic approaches to overcome cancer drug resistance. *Adv. Drug Deliv. Rev.* *65*, 1866–1879.
4. Giarra, S., Zappavigna, S., Campani, V., Abate, M., Cossu, A.M., Leonetti, C., Porru, M., Mayol, L., Caraglia, M., and De Rosa, G. (2018). Chitosan-Based Polyelectrolyte Complexes for Doxorubicin and Zoledronic Acid Combined Therapy to Overcome Multidrug Resistance. *Pharmaceutics* *10*, 180.
5. Sabourian, P., Yazdani, G., Ashraf, S.S., Frounchi, M., Mashayekhan, S., Kiani, S., and Kakkari, A. (2020). Effect of Physico-Chemical Properties of Nanoparticles on Their Intracellular Uptake. *Int. J. Mol. Sci.* *21*, 8019.
6. Mitchell, M.J., Billingsley, M.M., Haley, R.M., Wechsler, M.E., Peppas, N.A., and Langer, R. (2021). Engineering precision nanoparticles for drug delivery. *Nat. Rev. Drug Discov.* *20*, 101–124.
7. Abate, M., Scotti, L., Nele, V., Caraglia, M., Biondi, M., De Rosa, G., Leonetti, C., Campani, V., Zappavigna, S., and Porru, M. (2022). Hybrid Self-Assembling Nanoparticles Encapsulating Zoledronic Acid: A Strategy for Fostering Their Clinical Use. *Int. J. Mol. Sci.* *23*, 5138.

8. Lee, S.W.L., Paoletti, C., Campisi, M., Osaki, T., Adriani, G., Kamm, R.D., Mattu, C., and Chiono, V. (2019). MicroRNA delivery through nanoparticles. *J. Contr. Release* 313, 80–95.
9. Najahi-Missaoui, W., Arnold, R.D., and Cummings, B.S. (2020). Safe Nanoparticles: Are We There Yet? *Int. J. Mol. Sci.* 22, 385.
10. Gao, G., Guo, Q., and Zhi, J. (2019). Nanodiamond-Based Theranostic Platform for Drug Delivery and Bioimaging. *Small* 15, e1902238.
11. Karami, P., Salkhi Khasraghi, S., Hashemi, M., Rabiei, S., and Shojaei, A. (2019). Polymer/nanodiamond composites - a comprehensive review from synthesis and fabrication to properties and applications. *Adv. Colloid Interface Sci.* 269, 122–151.
12. Bartelmeß, J., Quinn, S.J., and Giordani, S. (2015). Carbon nanomaterials: multi-functional agents for biomedical fluorescence and Raman imaging. *Chem. Soc. Rev.* 44, 4672–4698.
13. Moore, L., Grobárová, V., Shen, H., Man, H.B., Míčová, J., Ledvina, M., Štursa, J., Nesladek, M., Fiserová, A., and Ho, D. (2014). Comprehensive interrogation of the cellular response to fluorescent, detonation and functionalized nanodiamonds. *Nanoscale* 6, 11712–11721.
14. Zhu, Y., Li, J., Li, W., Zhang, Y., Yang, X., Chen, N., Sun, Y., Zhao, Y., Fan, C., and Huang, Q. (2012). The biocompatibility of nanodiamonds and their application in drug delivery systems. *Theranostics* 2, 302–312.
15. Torelli, M.D., Nunn, N.A., and Shenderova, O.A. (2019). A Perspective on Fluorescent Nanodiamond Bioimaging. *Small* 15, e1902151.
16. Tinwala, H., and Wairkar, S. (2019). Production, surface modification and biomedical applications of nanodiamonds: A sparkling tool for theranostics. *Mater. Sci. Eng. C Mater. Biol. Appl.* 97, 913–931.
17. Torelli, M.D., Rickard, A.G., Backer, M.V., Filonov, D.S., Nunn, N.A., Kinev, A.V., Backer, J.M., Palmer, G.M., and Shenderova, O.A. (2019). Targeting Fluorescent Nanodiamonds to Vascular Endothelial Growth Factor Receptors in Tumor. *Bioconjugate Chem.* 30, 604–613.
18. Eldawud, R., Reitzig, M., Opitz, J., Rojanskul, Y., Jiang, W., Nangia, S., and Dinu, C.Z. (2016). Combinatorial approaches to evaluate nanodiamond uptake and induced cellular fate. *Nanotechnology* 27, 085107.
19. Rupaimoole, R., and Slack, F.J. (2017). MicroRNA therapeutics: towards a new era for the management of cancer and other diseases. *Nat. Rev. Drug Discov.* 16, 203–222.
20. Lu, J., Getz, G., Miska, E.A., Alvarez-Saavedra, E., Lamb, J., Peck, D., Sweet-Cordero, A., Ebert, B.L., Mak, R.H., Ferrando, A.A., et al. (2005). MicroRNA expression profiles classify human cancers. *Nature* 435, 834–838.
21. Misso, G., Di Martino, M.T., De Rosa, G., Farooqi, A.A., Lombardi, A., Campani, V., Zarone, M.R., Gullà, A., Tagliaferri, P., Tassone, P., and Caraglia, M. (2014). Mir-34: a new weapon against cancer? *Mol. Ther. Nucleic Acids* 3, e194.
22. Zhang, L., Liao, Y., and Tang, L. (2019). MicroRNA-34 family: a potential tumor suppressor and therapeutic candidate in cancer. *J. Exp. Clin. Cancer Res.* 38, 53.
23. Diener, C., Keller, A., and Meese, E. (2022). Emerging concepts of miRNA therapeutics: from cells to clinic. *Trends Genet.* 38, 613–626.
24. Rossi, M., Amodio, N., Di Martino, M.T., Caracciolo, D., Tagliaferri, P., and Tassone, P. (2013). From target therapy to miRNA therapeutics of human multiple myeloma: theoretical and technological issues in the evolving scenario. *Curr. Drug Targets* 14, 1144–1149.
25. Rossi, M., Amodio, N., Di Martino, M.T., Tagliaferri, P., Tassone, P., and Cho, W.C. (2014). MicroRNA and multiple myeloma: from laboratory findings to translational therapeutic approaches. *Curr. Pharmaceut. Biotechnol.* 15, 459–467.
26. Morelli, E., Leone, E., Cantafio, M.E.G., Di Martino, M.T., Amodio, N., Biamonte, L., Gullà, A., Foresta, U., Pitari, M.R., Botta, C., et al. (2015). Selective targeting of IRF4 by synthetic microRNA-125b-5p mimics induces anti-multiple myeloma activity in vitro and in vivo. *Leukemia* 29, 2173–2183.
27. Tagliaferri, P., Rossi, M., Di Martino, M.T., Amodio, N., Leone, E., Gulla, A., Neri, A., and Tassone, P. (2012). Promises and challenges of MicroRNA-based treatment of multiple myeloma. *Curr. Cancer Drug Targets* 12, 838–846.
28. Lionetti, M., Agnelli, L., Lombardi, L., Tassone, P., and Neri, A. (2012). MicroRNAs in the pathobiology of multiple myeloma. *Curr. Cancer Drug Targets* 12, 823–837.
29. Laube, C., Oeckinghaus, T., Lehnert, J., Griebel, J., Knolle, W., Denisenko, A., Kahnt, A., Meijer, J., Wrachtrup, J., and Abel, B. (2019). Controlling the fluorescence properties of nitrogen vacancy centers in nanodiamonds. *Nanoscale* 11, 1770–1783.
30. Huang, H., Dai, L., Wang, D.H., Tan, L.S., and Osawa, E. (2008). Large-scale self-assembly of dispersed nanodiamonds. *J. Mater. Chem.* 18, 1347–1352.
31. Krueger, A. (2008). New carbon materials: Biological applications of functionalized nanodiamond materials. *Chem. Eur J.* 14, 1382–1390.
32. Islam, N., Dihingia, A., Manna, P., Das, T., Kalita, J., Dekaboruah, H.P., and Saikia, B.K. (2019). Environmental and toxicological assessment of nanodiamond-like materials derived from carbonaceous aerosols. *Sci. Total Environ.* 679, 209–220.
33. Colvin, V.L. (2003). The potential environmental impact of engineered nanomaterials. *Nat. biotech.* 21, 1166–1170.
34. Jia, G., Wang, H., Yan, L., Wang, X., Pei, R., Yan, T., Zhao, Y., and Guo, X. (2005). Cytotoxicity of carbon nanomaterials: Single wall nanotube, multi wall nanotube and fullerene. *Environ. Sci. Technol.* 39, 1378–1383.
35. Schrand, A.M., Hens, S.A.C., and Shenderova, O.A. (2009). Nanodiamond Particles: Properties and Perspectives for Bioapplications. *Crit. Rev. Solid State Mater. Sci.* 34, 18–74.
36. Burns, R.C., and Davies, G.J. (1992). In *Properties of Natural and Synthetic Diamond*, J.E. Field, ed. (Academic Press), pp. 395–422.
37. Moustakas, T.D. (1994). In *Synthetic Diamond: Emerging CVD Science and Technology*, K.E. Spear and J.P. Dismukes, eds., pp. 145–192.
38. Dubrovinskaja, N., Dubrovinsky, L., Solopova, N.A., Abakumov, A., Turner, S., Hanfland, M., Bykova, E., Bykov, M., Prescher, C., Prakupenka, V.B., et al. (2016). Terapascal static pressure generation with ultrahigh yield strength nanodiamond. *Sci. Adv.* 2, e1600341.
39. Krueger, A., and Lang, D. (2012). Functionality is Key: Recent Progress in the Surface Modification of Nanodiamond. *Adv. Funct. Mater.* 22, 890–906.
40. Patnaik, S., and Gupta, K.C. (2013). Novel polyethylenimine-derived nanoparticles for in vivo gene delivery. *Expert Opin. Drug Deliv.* 10, 215–228.
41. Guo, S., Huang, Y., Jiang, Q., Sun, Y., Deng, L., Liang, Z., Du, Q., Xing, J., Zhao, Y., Wang, P.C., et al. (2010). Enhanced gene delivery and siRNA silencing by gold nanoparticles coated with charge-reversal polyelectrolyte. *ACS Nano* 4, 5505–5511.
42. Shahbazi, R., Ozpolat, B., and Ulubayram, K. (2016). Oligonucleotide-based therapeutic nanoparticles in cancer therapy. *Nanomedicine* 11, 1287–1308.
43. Krivohlavá, R., Neuhöferová, E., Jakobsen, K.Q., and Benson, V. (2019). Knockdown of microRNA-135b in Mammary Carcinoma by Targeted Nanodiamonds: Potentials and Pitfalls of In Vivo Applications. *Nanomaterials* 9, 866.
44. Claveau, S., Kindermann, M., Papine, A., Díaz-Riascos, Z.V., Délen, X., Georges, P., López-Alemany, R., Tirado, Ö.M., Bertrand, J.R., Abasolo, I., et al. (2021). Harnessing subcellular-resolved organ distribution of cationic copolymer-functionalized fluorescent nanodiamonds for optimal delivery of active siRNA to a xenografted tumor in mice. *Nanoscale* 13, 9280–9292.
45. Schrand, A.M., Huang, H., Carlson, C., Schlager, J.J., Omacr Sawa, E., Hussain, S.M., and Dai, L. (2007). Are diamond nanoparticles cytotoxic? *J. Phys. Chem. B* 111, 2–7.
46. Wang, L., Su, W., Ahmad, K.Z., Wang, X., Zhang, T., Yu, Y., Chow, E.K.-H., Ho, D., and Ding, X. (2022). Safety Evaluation of Nanodiamond Doxorubicin Complexes in a Naïve Beagle Canine Model Using Hematologic, Histological, and Urine Analysis. *Nano Res.* 15, 3356–3366.
47. Perevedentseva, E., Hong, S.F., Huang, K.J., Chiang, I.T., Lee, C.Y., Tseng, Y.T., and Cheng, C.L. (2013). Nanodiamond internalization in cells and the cell uptake mechanism. *J. Nanoparticle Res.* 15, 1834.
48. Faklaris, O., Garrot, D., Joshi, V., Druon, F., Boudou, J.P., Sauvage, T., Georges, P., Curmi, P.A., and Treussart, F. (2008). Detection of single photoluminescent diamond nanoparticles in cells and study of the internalization pathway. *Small* 4, 2236–2239.
49. Nie, L., Zhang, Y., Li, L., van Rijn, P., and Schirhagl, R. (2021). pH Sensitive Dextran Coated Fluorescent Nanodiamonds as a Biomarker for HeLa Cells Endocytic Pathway and Increased Cellular Uptake. *Nanomaterials* 11, 1837.
50. Wang, C., Jia, Q., Guo, X., Li, K., Chen, W., Shen, Q., Xu, C., and Fu, Y. (2022). microRNA-34 family: From mechanism to potential applications. *Int. J. Biochem. Cell Biol.* 144, 106168.

51. Yuan, Y., Chen, Y., Liu, J.H., Wang, H., and Liu, Y. (2009). Biodistribution and fate of nanodiamonds in vivo. *Diam. Relat. Mater.* 18, 95–100.
52. Van der Laan, K., Hasani, M., Zheng, T., and Schirhagl, R. (2018). Nanodiamonds for In Vivo Applications. *Small* 14, e1703838.
53. Guessous, F., Zhang, Y., Kofman, A., Catania, A., Li, Y., Schiff, D., Purow, B., and Abounader, R. (2010). microRNA-34a is tumor suppressive in brain tumors and glioma stem cells. *Cell Cycle* 9, 1031–1036.
54. Zhao, H., Chen, S., Gao, K., Zhou, Z., Wang, C., Shen, Z., Guo, Y., Li, Z., Wan, Z., Liu, C., and Mei, X. (2017). Resveratrol protects against spinal cord injury by activating autophagy and inhibiting apoptosis mediated by the SIRT1/AMPK signaling pathway. *Neuroscience* 348, 241–251.
55. Chakraborty, S., Datta, S., and Ghosh, S. (2019). Induction of autophagy under nitrosative stress: A complex regulatory interplay between SIRT1 and AMPK in MCF7 cells. *Cell. Signal.* 64, 109411.
56. Lau, A.W., Liu, P., Inuzuka, H., and Gao, D. (2014). SIRT1 phosphorylation by AMP-activated protein kinase regulates p53 acetylation. *Am. J. Cancer Res.* 4, 245–255.
57. Maiuri, M.C., Criollo, A., and Kroemer, G. (2010). Crosstalk between apoptosis and autophagy within the Beclin 1 interactome. *EMBO J.* 29, 515–516.
58. Liao, H., Xiao, Y., Hu, Y., Xiao, Y., Yin, Z., Liu, L., Kang, X., and Chen, Y. (2016). Methylation-induced silencing of miR-34a enhances chemoresistance by directly up-regulating ATG4B-induced autophagy through AMPK/mTOR pathway in prostate cancer. *Oncol. Rep.* 35, 64–72.
59. Cao, Z., Kon, N., Liu, Y., Xu, W., Wen, J., Yao, H., Zhang, M., Wu, Z., Yan, X., Zhu, W.G., et al. (2021). An unexpected role for p53 in regulating cancer cell-intrinsic PD-1 by acetylation. *Sci. Adv.* 7, eabf4148.
60. Wong, S., and Weber, J.D. (2007). Deacetylation of the retinoblastoma tumour suppressor protein by SIRT1. *Biochem. J.* 407, 451–460.
61. Sirangelo, I., Borriello, M., Liccardo, M., Scafuro, M., Russo, P., and Iannuzzi, C. (2021). Hydroxytyrosol Selectively Affects Non-Enzymatic Glycation in Human Insulin and Protects by AGEs Cytotoxicity. *Antioxidants* 10, 1127.
62. Tavera-Mendoza, L.E., and Brown, M. (2017). A less invasive method for orthotopic injection of breast cancer cells into the mouse mammary gland. *Lab. Anim.* 51, 85–88.